Direct measurement of the $\bar{K}N \to \pi\Sigma$ scattering amplitude below the $\bar{K}N$ threshold employing the $d(K^-, N)"\pi\Sigma"$ reaction

Kentaro Inoue

August 3, 2022

Contents

Chapter 1

Experimental setup

1.1 Experimental facility

1.1.1 J-PARC

Our experiment was performed at the K1.8BR beamline at hadron facility of the J-PARC located at the Tokai site in Ibaraki Prefecture [28, 29]. J-PARC, which means Japan Proton Accelerator Research Complex, consists of some facilities, which are nuclear transmutation facility, materials, and life experimental facility, muon facility, neutrino facility, and hadron facility. The concept of the J-PARC is to provide various secondary beam for the above purpose. The J-PARC has three accelerators, first one is linac which is injector and accelerates proton beam to $400MeV/c$, second is RCS (Rapid Cycling Synchrotrons) which accelerates proton beam to $3GeV$, which was provided to materials and life experimental facility and muon facility. Next is MR (Main Ring) which accelerates proton beam to $30GeV/c$, which beam was extracted by two methods. One is the fast extraction (FX) for the neutrino facility to produce a neutrino beam which transported to the super Kamiokande. The other is the slow extraction (SX) for the hadron facility. In this extraction, banched beam in the MR is gradually extracted as scraping. For this purpose, the $30GeV/c$ proton beam was extracted about 2-second with a 5.2-second repetition cycle.

This continuous beam is irradiated on the primary target that is 6mm × 6mm × 66mm golden block to generate secondary beam which includes anti-proton, pion, kaon and so on that is not naturally exist. The secondary beam was transported to several beamlines.

The present experiment was performed at the K1.8BR beamline, which was placed at north of the hadron facility and branced from the K1.8 beamline which was optimized for beam whose momentum is around $1.8GeV/c$.

1.1.2 K1.8BR beam line

The K1.8BR beamline was planned to use low momentum kaon beam whose upper limit is 1.2 GeV/c. Such kaon decays with short decay time, so beam line length should be short. So, our beamline length was designed at about 31m by branching the K1.8 beamline. Fig 1.1 shows a schematic view of the K1.8BR beamline.

The D1 magnet accumulates secondary particles with the 6-degree aperture and the D2 magnet selects a specific momentum beam with $\pm$ 3% momentum bite. Intermediate focus slit (IF Slit) defined beam profile to increase the number of kaon beam while keeping good kaon and another particle ratio. Kaon and other particles were separated by the electrostatic separator (ES1) using vertical direction statical electronic field which uses the principle that different mass charged particles pass different trajectories by the electrical field. The kaon beam was kicked up by the CM1 magnet, was bent in the opposite direction by ES1 and was kicked to parallel direction by the CM2 magnet. Other particles pass through different position of vertical direction at mass slit1 (MS1), so these were intercepted by the MS1. Also, the horizontal directional slit of the MS1 defines the dispersive of the beam. The D3 magnet switched beam to the K1.8 or the K1.8BR. After the D3 magnet, an SQDQD system is employed to focus the beam on the experimental target at FF of the K1.8BR beam line. The first-order beam envelope calculated by the TRANSPORT code [30] is shown in Fig 1.2.

The data for the $d(K^-, p)$ has been taken in May-June in 2016 which is so-called as MR-RUN69 and the data for the $d(K^-, n)$ has been taken in Jan-Feb in 2018 which is so-called as MR-RUN78.
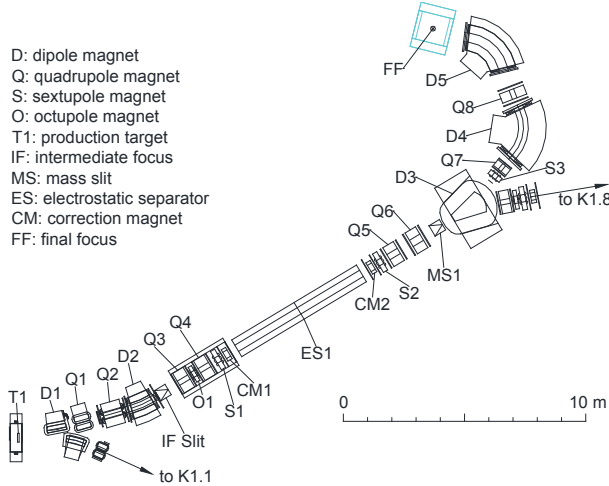

Figure 1.1: Schematic view of the K1.8BR beam line.

Table 1.1: Parameters of the beam-line magnets. D5 field is a typical monitored value. Other field values are interpolations of measured points.

Element	J-PARC designation	Gap or bore/2 (cm)	Effective length (cm)	Bend (deg)	Current (A)	Field at pole (kG)
D1	5C216SMIC	8	90.05	10	-369	-6.7444
Q1	NQ312MIC	8	67.84		-357	-3.075
Q2	Q416MIC	10	87.04		-668	3.872
D2	8D218SMIC	15	99.65	15	-698	-8.7673
IF-H	Movable horizontal slit for acceptance control					
IF-V	Movable vertical slit, $(y|\phi)=0$					
Q3	Q410	10	54.72		-679	-4.108
O1	O503	12.5	15		-15	-0.29
Q4	Q410	10	54.72		-776	4.692
S1	SX504	12.5	27.6		-42	-0.29
CM1	4D604V	10	20	(0.856)	348	1.633
ES1	Separator	10	600		E=-500 kV/10 cm	
CM2	4D604V	10	20	(0.856)	348	1.630
S2	SX504	12.5	27.6		-136	1.02
Q5	NQ510	12.5	56		-498	4.218
Q6	NQ610	15	57.2		-535	-4.316
MOM	Movable horizontal slit for momentum acceptance control					
MS1	Movable vertical slit for K-π separation					
	$(y|\phi)=0$, $(y|y)=0.844$, $(y|\theta\phi)=(y|\phi\delta)=0$					
D3	6D330S	15	165.1	20	210	-7.064
S3	SX404	10	20		-34	-1.062
Q7	Q306	7.5	30.34		-464	4.026
D4	8D440S	20	198.9	60	-1938	-17.906
Q8	NQ408	10	46.5		-110	0.671
D5	8D240S	20	195.9	55	-1666	-16.437

Primary beam momentum	30 GeV/c proton
Primary beam power	50kW
Proton per spill	4.8×10^{13}
Repetition cycle	5.2 sec
Spill Length	2 sec
Spill suty factor	50%
Spill extraction efficiency	99.5 %
Production target	Au(50 % loss)
Production angle	6 degrees
Length (T1-FF)	31.3 m
Momentum range	1.2 GeV/c max.
Acceptance	2.0 msr·% ($\Delta\Omega \cdot \Delta p/p$)
Momentum bite	$\pm$ 3 %

Table 1.2: Parameters of the K1.8BR beamline and typical operation condition
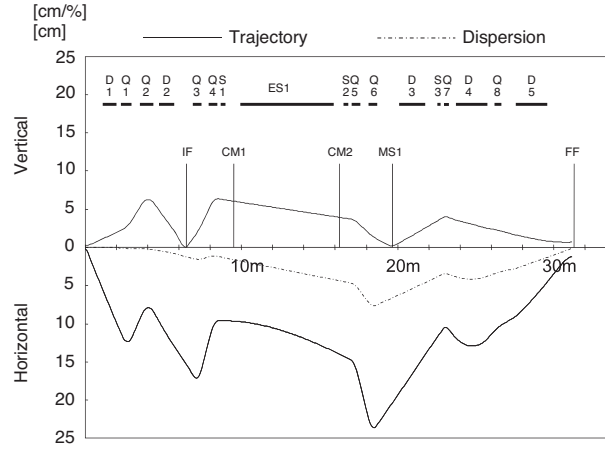

Figure 1.2: First-order beam envelope calculated by the TRANSPORT.

1.2 Beam line detectors
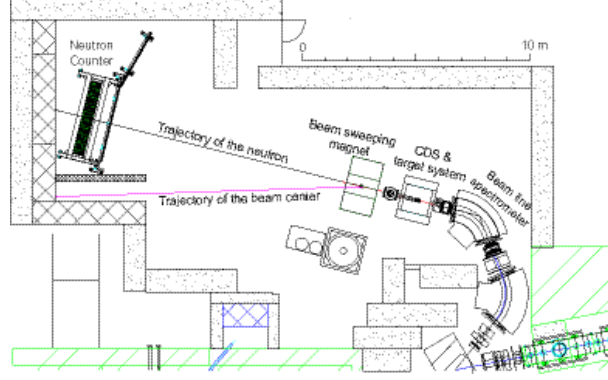
1.2.1 Overview

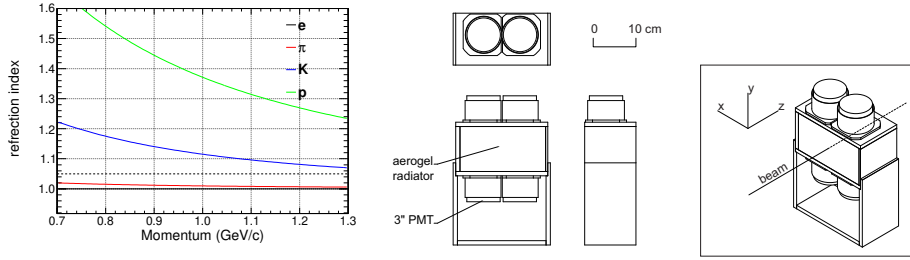Figure 1.3: Schematic view of the experimental hall at the K1.8BR.

Figure 1.4: The right figure shows a schematic drawing of the AC. The left figure represents the threshold of reflection index for Cherenkov radiation and the momentum. The horizontal dotted line shows the reflection index of the Aerogel (n=1.05).

A kaon was identified by threshold type of aerogel Cherenkov counter (AC) with refractive index $n = 1.05$ which can identify kaon and pion around $0.7 \sim 1.2 GeV/c$ as Fig1.4. This offline level identification information was used for beam line tuning, especially koan and another particle separation. We first search ES1 voltage and CM1/2 current which maximize kaon yield. After that, IF slit and MS1 slit were adjusted to maximize the number of kaons while keeping an acceptable level of pion contamination. In this tuning, vertical direction opening width was decided to avoid pion peak come from direct production at the T1 target and horizontal direction was set to reject pion come from magnets and so on installed in beamline which so-call pion hallo.

The beam particle identification was also performed using the TOF

method by beamline hodoscope counter (BHD) and time-zero (T0) counter
which has about $7.7m$ flight length. The T0 counter was installed at down-
stream of D5 magnet and was rotated by 45 degrees about the beam direc-
tion axis, which consists of 5 segmented plastic scintillation counters whose
size is 160mm (height) × 32mm (width) × 10mm (thickness), so the T0
counter covers 160mm × 160mm effective area. A counter uses the Saint-
Gobain BC420 scintillator and attached readout which is 3/4 inch Hama-
matsu H6612B photomultipliers to both sides of the scintillator.

The BHD counter was installed at just upstream of the D4 magnet, which
consists of 20 segment plastic scintillaton counters whose size is 160mm
(height) × 20mm (width) × 5mm (thickness), so the BHD counter covers
400mm (horizontal) × 160mm (vertical) effective area. A counter uses the
same photomultipliers as the T0 counter. Since beam rate was a few M
events per spill, photomultipliers were attached high voltage booster to the
last three dynodes to avoid gain drop due to high current by high rate beam.

1.2.2   Beam momentum analyzer

Beam momentum was reconstructed from the second-order transfer matrix
of the D5 magnet, whose magnetic field was monitored during the exper-
iment with high-precision Hall probe Lakeshore 475 which has $\sim 10^{-5}$ T
resolution. The fluctuation of the magnetic field was $\sim 2 \times 10^{-4}$ that cor-
respond to $0.2GeV/c$ for $1GeV/c$ beam. Also, helium bag was install at
pass way of the D5 magnet to suppress the multiple scattering effect due to
materials.

For measuring tracks of upstream and downstream of the D5 magnet,
planer type drift chambers were installed at these positions. These chambers
were named the BLC1 and the BLC2 which has two components, BLC1a/b
and BLC2a/b, respectively. These chamber sets were rotated 45 degrees
about the beam direction axis. All components have the $UU'VV'UU'VV'$
configuration and 32 sense wires pre layer, so each component has 256 read-
out channels. Drift lengths of the BLC1 and the BLC2 are 4mm and 2.5mm
which corresponds to cover 252mm × 252mm and 157.5mm × 157.5mm
area, respectively. These drift chambers use 12.5 μm diameter gold-plated
tungsten wires with 3% rhenium for sense wires and 75 μm diameter copper-
beryllium wires for potential wires. The cathode planes made of 12.5 μm
aluminized Kapton. The spatial resolution was evaluated at about 200
μm which was estimated at 10^{-3} corresponding to $1GeV/c$ for $0.1GeV/c$
beam. These drift chambers use isobutane and argon including methylal
(dimethoxy-methane) to pass through its bubbler whose temperature is 4
°C in the refrigerator mixed to 1:4 by the mass-flow controller. As a result,
the ratio of isobutane, argon and methylal was 20%, 76% and 4%.

1.2.3 BPD

BPD which means backward proton detector was developed for the measurement of backward proton decay from Λ in $Y^* \to \pi^0 \Sigma^0 \to \pi^0 \gamma \pi^0 \Lambda$ decay scheme which was installed at most upstream of the CDS. The scattered angle of Y^* is enhanced backward scattering, especially below the threshold due to small momentum transfer. The BPD was installed to obtain large acceptance for these protons. The BPD is a plastic scintillator hodoscope array with a size of 350mm (horizontal) $\times$ 340mm (vertical). It is segmented into 70 units of 5mm $\times$ 5mm $\times$ 340mm scintillation counter made of Eljen EJ-230. Two MPPCs with a 3mm$\times$3mmm sensitive area (Hamamatsu S10362-33-050C) were directly put on both sides of each slab. The present thesis explains the $\pi^\mp \Sigma^\pm$ and the $d(K^-, p)"\pi^- \Sigma^0"$ modes analysis, so BPD was used only energy loss calculation.
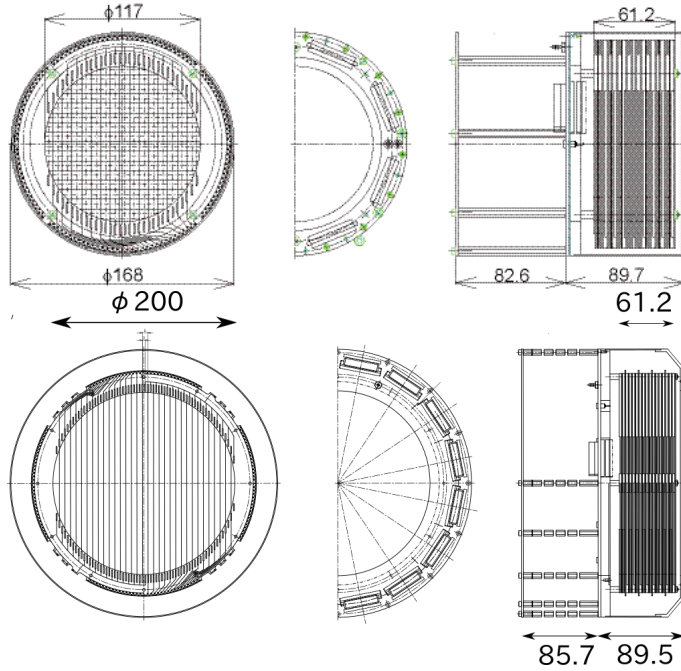
1.2.4 Vertex chamber - BPC

Figure 1.5: Schematic view of the BPC. Above figure shows about MR-RUN69. Bottom figure shows about MR-RUN78.

BPC which means backward proton chamber was developed for the measurement of backward proton decayed from hyperons that come from $\pi^0 \Sigma^0$ mode. The BPC also used beam tracking at just upstream of the experimental target for the definition of reaction vertex point. The BPC was installed at just upstream of the experimental target where is in the CDS

described after. The BPC is a planer type drift chamber which has a circular plane to maximize effective area in limited space. The BPC configuration is XX'YY'XX'YY', so the BPC has 8 layers.

In MR RUN69, the chamber with 168mm diameter outer which has 15 sense wires per layer with 3.6mm drift length corresponding to 111.6mm effective area was used as the BPC. In this run, the inner hodoscope (IH) was installed in CDS for the trigger counter to evaluate CDC efficiency.

In MR RUN78,the IH was removed to maximize acceptance of backward proton so larger chamber was used as the BPC whose outer size is 290mm diameter and 32 sense wires per layer with 3.0mm drift length corresponding to 189mm effective area.

These chambers were used 50μm diameter copper-beryllium wire for potential wires and 12.5μm diameter gold-plated tungsten. These cathode planes are made of 9μm carbon aramid foil. These are 120 read-outs and 256 read-outs in MR-RUN69 and MR-RUN78, respectively.
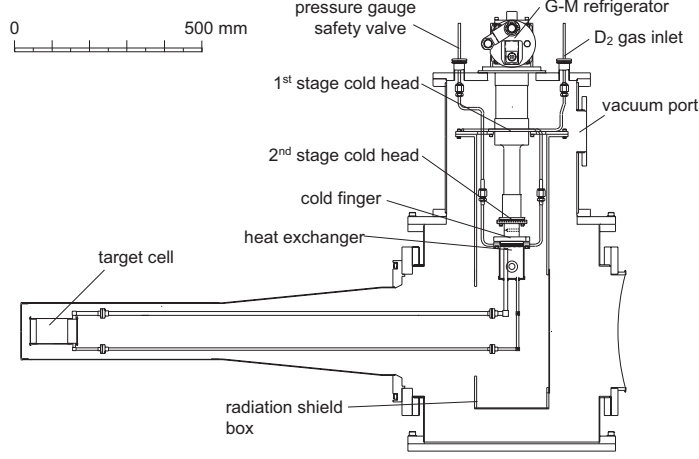
1.2.5   Beam definition counter

The beam definition counter (DEF) was installed just upstream of the target the vacuum chamber for the definition of the beam to avoid particle not hitting the liquid deuterium target. In our beamline, a half of kaon hits the experimental targets due to large beam size. High trigger rate not only is the cause of low data quality but also the cause of decreasing DAQ efficiency due to computer busy, so the DEF signal was coincided with beam trigger made by the T0 and BHD and was used reducing beam trigger rate. The trigger rate was successfully suppressed by about 30% by this counter.

1.3   Target system

1.3.1   Luquid D_2 target system

A side view of the cryostat for the liquid D_2 target is shown in Fig1.6. Deuterium was stored $1000l$ in a tank as gases which is room temperature and 2 atm keeping positive pressure after liquefaction for avoiding contamination from other materials. The D_2 gas is fed into the cryostat through the top flange. Cooling of D_2 was performed by the Gifford–McMahon (G–M) refrigerator (Sumitomo Heavy Industries, Ltd., RDK-145D and CSA-71A) built into the cryostat. The cooling was performed by 2-step. The cooling power at the first and second stages is $35W$ at 50K and $1.5W$ at $4.2K$, respectively. A copper plate was anchored to the first-stage cold head of the G-M refrigerator in inlet pip for the pre-cooling of the D_2. Another inlet pipe was directly connected through the top flange to the head exchanger for measuring the pressure of the D_2 target inside of the heat exchanger. Since this pipe has a larger conductance, a safety valve that prevents a

Figure 1.6: Schematic drawing of the liquid D_2 cryostat.

sudden pressure rise is also connected to it. The D_2 gas is cooled in the heat exchanger where the second stage of the G–M refrigerator is thermally contacted.
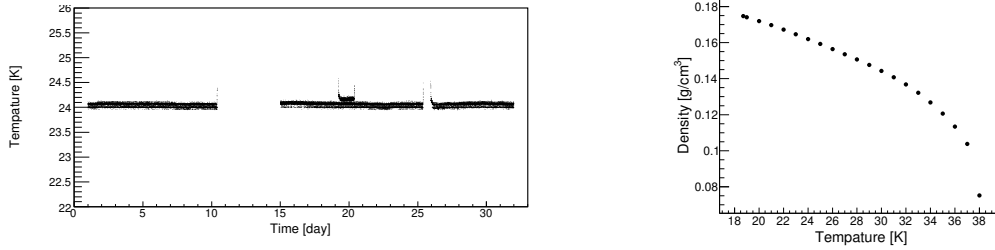

Figure 1.7: The left figure shows the temperature of the D_2 target. The right figure shows the relation of the density and the D_2 temperature at 1 atm.

The target cell was $6.8cm$ diameter and $12.5cm$ length cylinder made of PET. Liquifregrated D_2 was transferred by downpipe and warmed liquid D_2 by the heat load was returned through the upper pipe, so the heat was effectively transferred between the target cell and the heat exchanger [33]. Since the temperature range of liquid D_2 is narrow as 18.7-23.8K at 1 atm, the temperature of the D_2 should be controlled in the liquid range to avoid blocking due to the solid D_2. Since the cooling power of the second stage of the G–M refrigerator is larger than the heat load on the low-temperature parts, we have installed a heater near the cold finger to compensate for the heat load. The current in the heater is controlled by a proportional-

integral-derivative (PID) algorithm with an input of the temperature of the heat exchanger. Target cell temperature in MR-RUN78 was represented in Fig1.7 which was monitored by Pt-Co thermometer (CHINO R800-6) whose tolerance was $\pm$ 0.5K. The same figure also shows the relation of temperature and density of D_2 at 1 bar. The error of D_2 density was estimated at $1.5 \times 10^{-3}[g/cm^3]$ from tolerance and fluctuation.

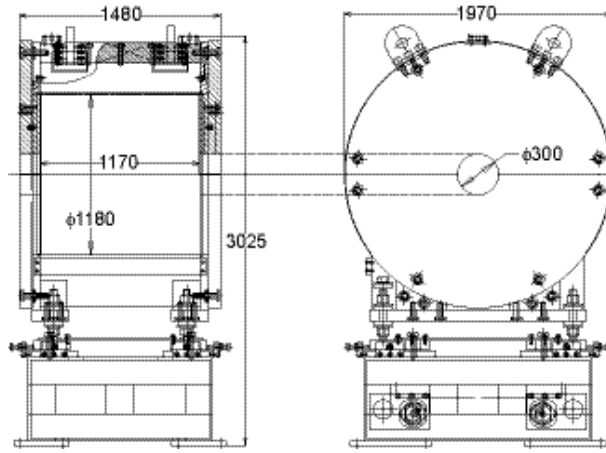## 1.4   The cylindrical detector system

Figure 1.8:   Design of the solenoid magnet (all dimensions in mm)

The cylindrical detector system (CDS) surrounds the experimental target system to measure produced charged particles. The CDS consists of three parts, the outermost part is the solenoid magnet to make the uniform magnetic field for momentum analysis, next is the cylindrical detector hodoscope (CDH) to measure time-of-flight from the T0 and make trigger signal, and the cylindrical drift chamber (CDC) to measure the trajectory in the magnetic field, by which the momentum of a charged particle was analyzed. Particle identification was performed by the momentum and T0-CDH TOF.

1.4.1   Solenoid magnet

The CDS is a solenoid type spectrometer whose bore diameter is 1.18m and the length is 1.17m with an overall weight is about 23 tons. The design of the solenoid magnet is shown in Fig1.8. The magnet provides a uniform field strength inside the tracking volume ($|z| < 420mm$). In the present experiment, it is operated at 0.7T.
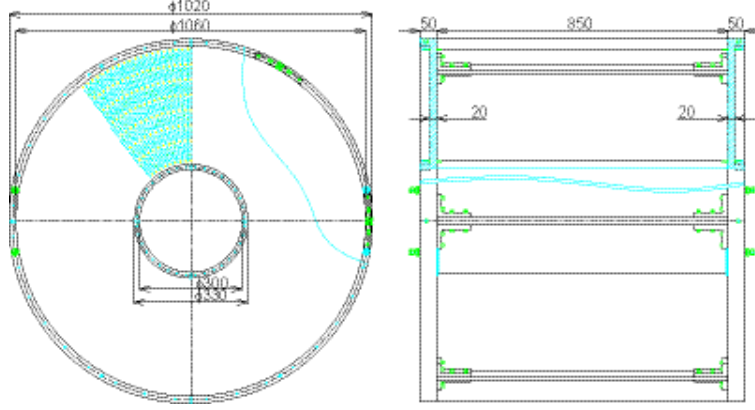
1.4.2 Cylindrical drift chamber

Figure 1.9: Design of the CDC (all dimensions in mm). The CDC consists of two aluminum end-plates, a 1mm thick CFRP cylinder as an inner wall, and six aluminum posts that are placed outside the tracking volume.

Figure 1.10: Cell structure of the CDC.

The CDC is a cylindrical wire drift chamber that contains 15 layers of anode wires. The structure of the CDC is shown in Fig1.9. The outer radius is 530mm and the inner radius is 150mm, with a total length of 950mm. The wire length of axial layers is 833.8mm, thus the angular coverage is $49° < \theta < 131°$ in the polar angle region corresponding to a solid angle coverage of 66% of 4π. The CDC consists of two aluminum end-plates of 20mm thickness, a 1mm thick CFRP cylinder as the inner wall of the CDC,

Table 1.3: Wire configuration of the CDC.

super layer	layer	wire direction	radius (mm)	cell width (degree)	cell width (mm)	stereo angle (degree)	signal channels per layer
A1	1	X	190.5	5.00	16.7	0	72
	2	X'	204.0		17.8	0	
	3	X	217.5		19.0	0	
U1	4	U	248.5	4.00	17.3	-3.55	90
	5	U'	262.0		18.3	-3.74	
V1	6	V	293.0	3.60	18.4	3.77	100
	7	V'	306.5		19.3	3.94	
A2	8	X	337.5	3.00	17.7	0	120
	9	X'	351.0		18.4	0	
U2	10	U	382.0	2.40	16.0	-3.28	150
	11	U'	395.5		16.6	-3.39	
V2	12	V	426.5	2.25	16.7	3.43	160
	13	V'	440.0		17.3	3.54	
A3	14	X	471.0	2.00	16.4	0	180
	15	X'	484.5		16.9	0	

and six aluminum posts that are placed outside the tracking volume. The CDC uses gold-plated tungsten of 30μm ϕ for the sense wires, and gold-plated aluminum of 100μm ϕ for the field and guard wires. These wires are supported by feedthroughts with a bushing inserted at the end. Bushes with an 80 and 200μm ϕ hole are used for the sense and field/guard wires, respectively.

The CDC has 15 layers of small hexagonal cells with a typical drift length of 9mm, which are grouped int 7 super layers as shown in Fig1.10. Table 1.3 gives the detailed parameter of the wire configuration. The layers are in the radial region from 190.5mm (layer 1) to 484.5mm (layer 15). The 8 stereo layers tilted by about $3.5°$ are used to obtain longitudinal position information. The number of readout channels is 1816 and the total number of wires in the CDC is 8064.

The drift gas is 1 atm of mixed argon (50%)-ethane (50%). A high voltage is applied to the field and guard wires, and the sense wires are kept at ground potential. For the first super-layer (A1) and the second one (U1), a high voltage of -2.8kV is applied to the potential wires, and -2.7kV to the potential wires of the other super-layers. Also, -1.5kV, -1.8kV, and -0.6kV are applied to the innermost, the outermost, and the other guard wires, respectively.

1.4.3 Cylindrical detector hodoscope

The CDH is a segmented plastic scintillation counter used for the charged particle trigger and particle identification. The CDH is located at a radius

of 544mm from the beam axis covering a polar angle range from 54 to 126 degree corresponding to a solid angle coverage of 59% of 4π.

The CDH consists of 36 modules, individually mounted on the inner wall of the solenoid magnet. The scintillators are mode of ELJEN EJ-200, with dimensions of 790mm in length, 99mm in width, and 30mm in thickness. The scintillation light is transferred through light guides to a pair of Hamamatsu R7761 fine-mesh 19-dynode photomultipliers 1.5 inches in diameter.

The CDH is operated in the 0.7T magnetic field with a typical PMT gain of $\sim 10^6$. The measured average time resolution of the CDH without a magnetic field is 71 ± 3 ps (σ), obtained with cosmic ray data. The error represents the variation among the segments.

1.4.4 Inner hodoscope

An inner hodoscope (IH) is a segmented plastic scintillation counter mounted on the inner wall of the CFRP cylinder of the CDC at a radius of 140mm from the beam axis. The IH consists of 24 ELJEN EJ-200 scintillators with a dimension of 600mm in length, 27mm in width, and 3mm in thickness. Each segment is overlapped by 1mm due to the strong magnetic field and limited space, multi-pixel photon counters (MPPCs) with a 3mm × 3mm sensitive area were used (Hamamatsu S10362-33-100C). The scintillation light is collected by 4 wavelength-shifting fibers embedded in the scintillator and connected to an MPPC with a specially designed connector. The MPPC signal is read out by using a preamplifirer.

The IH was used as a trigger counter for the efficiency estimation of the CDC. The IH was removed in MR RUN78 to increase acceptance for the backward scattered proton.

1.5 Forward detector systems

Beam pass through the target was swept to the beam dump direction by the beam sweep magnet called Ushiwaka, which also used to sweep positive charged particles to the opposite direction of the beam.
The neutron counter array (NC) was placed at about 15m downstream of the target to detect neutral particles and measure its velocity by TOF method. The charged particle was rejected by the beam veto counter (BVC) and the charged veto counter (CVC), which was installed at just upstream of the Ushiwaka and the NC, respectively. The proton counter was located at the opposite position of the beam dump to measure positive charged particles. Half of the CVC was also used for a positive charged particle. Because the trajectory of the charged particle depends on its momentum, the forward drift chamber was installed at upstream of the Ushiwaka magnet to decide its trajectory. The momentum of forward positive charged particle was evaluated by the TOF method.

1.5.1 Beam sweeping magnet

The Ushiwaka placed at 250cm downstream of the target has a large aperture which of 82cm (horizontal) × 40cm (vertical) and a pole length of 70cm, which is larger than the acceptance of the NC. The Ushiwaka can be applied to 1.6T at maximum value.
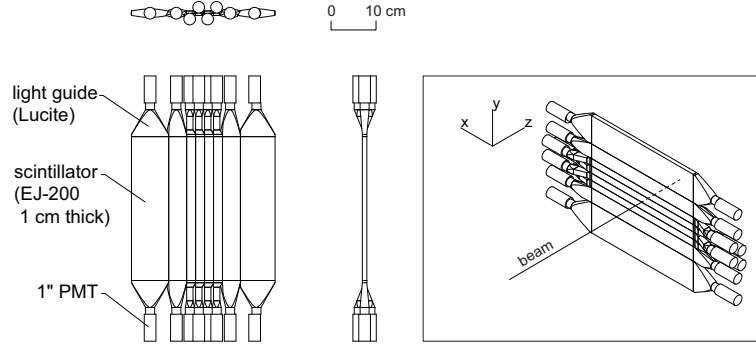
1.5.2 Beam veto counter

Figure 1.11:   Schematic view of the BVC.

The BVC was attached on the downstream flange of the target cryostat to reject charged particle contamination to neutral trigger, especially come from beam particle pass through. The coverage size of the BVC is 320mm (height) × 320mm (width) × 10mm (thickness) made of ELJEN EJ-200. This size is large enough to cover the acceptance of the neutron counter. The BVC is horizontally segmented int 8units with different sizes as shown in Fig1.11 to avoid the over-concentration to the beam on the central segments. In this position, there is some leak magnetic field from the solenoid magent of the CDS and the Ushiwaka magnet so its read-out used 1-inch fine-mesh Hamamatsu R5505 photomultipliers which were attached on both ends of each scintillator segment through Lucite light guides.

1.5.3 Neutron counter array

The neutron counter array was placed at 14.7m downstream of the target to measure neutron comes from $d(K^-, n)$ reaction. The NC consist of 7 layers and each layer has 16 segmented plastic scintillator whose size is 20cm (width) × 150cm (height) × 5cm (thickness). The NC is covered 6.2° in horizontal and 2.9° in vertical. The scintillators for the first 3 layers are made of Saint-Gobain BC408 and the other four layers are made of Saint-Gobain BC412. 2 inch Hamamatsu H6410 photomultipliers were attached to both sides of the scintillator through a Lucite light guide. The average time resolution of the neutron counter, measured with cosmic rays, is 92 ± 10 ps

(σ). The error represnets variation among the segments. Detection efficiency about $1.0GeV/c$ neutron was estimated by $K^-p \to K^0n$ reaction using H_2 target which is described Sec.**??**

1.5.4 Charge veto counter

The charged veto counter (CVC) was placed at just upstream of the NC for the rejection of charged particles in the NC. The CVC consists of 34 segmented plastic scintillators whose size is 10cm (width) $\times$ 150cm (height) $\times$ 5cm (thickness). The scintillator was attached 2 inch Hamamatsu H6410 photomultipliers trough the Lucite light guide. The scintillator is of Eljen EJ-200 type. The average time resolution measured with cosmic rays is 78 ± 7 ps (σ). The error represents the variation among the segments. Half of the CVC counter was used for the forward proton measurement.

1.5.5 Proton counter

The proton counter (PC) was placed at opposite side of beam sweeping direction to measure inflight-(K^-, p) reaction. The PC consists of 27 segmented plastic scintillators whose size is the same as the CVC. The PC has 2.7m (horizontal) and 1.5m (vertical) effective area. The scintillators made of Saint-Gobian BC408. The Hamamatsu H6410 was attached both side of scintillator through the Lucite light guide.

1.5.6 Forward drift chamber

The forward drift chamber (FDC1) was attached to the Ushiwaka magnet to measure the trajectory of the forward proton before sweeping for the decision of flight-length. The FDC1 is a planer type dift chamber that has 6 layers consists of UU'-XX'-VV'. UU' and VV' layers were tilted $\pm30°$ about the beam axis. Each layer has a 6mm gap in each sense wires and each pair plane was located at 20mm.

1.6 Data acquisition

1.6.1 Overview

In this section, the data accumulated system was explained. This experiment mainly used hodoscopes and drift chambers. Hodoscope output split into two signals. a signal direct send to the ADC (Analog-Digital-Converter). another signal was discriminated against with some thresholds and send to the TDC(Time-Digital-Converter) that was also used as a trigger signal. Up and down readout of hodoscopes which has double readout was made coincided singal to make trigger singal.

Table 1.4: Summary of the beam-line chamber parameters.

	BLC1a	BLC1b	BLC2a	BLC2b
number of planes	8	8	8	8
plane configuration	UU'VV'UU'VV'	UU'VV'UU'VV'	UU'VV'UU'VV'	VV'UU'VV'UU'
number of sense wires in a plane	32	32	32	32
wire spacing (mm)	4	4	2.5	2.5
effective area (mm)	256×256	256×256	160×160	160×160
Sense wire				
material		Au-plated W (3% Re)		
diameter (μm)		12		
Potential wire				
material		Au-plated Cu-Be		
diameter (μm)		75		
Cathode plane				
material		alminized-Kapton		
thickness (μm)		12.5		
operation voltage				
potential	-1.25	-1.25	-1.25	-1.25
cathord	-1.25	-1.25	-1.25	-1.25

	BPC(Run68)	BPC(Run78)	FDC1
number of planes	8	8	6
plane configuration	XX'YY'X'XY'Y	XX'YY'X'XY'Y	UU'XX'VV'
number of sense wires in a plane	15	32	64
wire spacing (mm)	3.6	3	3
effective area (mm)	111.6ϕ	189ϕ	
Sense wire			
material		Au-plated W (3% Re)	
diameter (μm)		12	12
Potential wire			
material		Au-plated Cu-Be	Au-plated Cu-Be
diameter (μm)		75	75
Cathode plane			
material		Cu aramid	alminaized-Kapton
thickness (μm)		9	7.5
operation voltage			
potential	-1.50	-1.45	-1.45
cathord	-1.50	-1.45	-1.45

These trigger signals were combined to make various conditions for data taking. Data taking scheme was consist of TKO creats [31] which has ADC and TDC modules to accumulate digital data which were controlled by VME-SMPs (supper memory partner) via a TKO SCH (supper controller head [32]. This system was operated by the Linux PC.

1.6.2 Trigger circuit

We took some triggered data in which one is beamline level to evaluate beam status and the other is the reaction required level for the specific physics. These were two timing trigger signals, one was a fast signal which was come from the beamline and the CDS and another one was about 100ns late signal which comes from forward counters. The fast signal can be made faster trigger than data signals, although late signal can not be made such a fast trigger signal. So, fast trigger signals deciding whether to accumulate the data is so-called as 1st level decision trigger and late trigger signals deciding whether to transfer the data to the PC was so-called as 2nd level decision trigger. Trigger scheme was shown in Fig1.14.

Beam trigger was a coincidence of the BHD and the T0. Beam particle was identified whether to pion or kaon by the AC installed just downstream of the T0 that also required the DEF signal to guarantee that beam was actually irradiated on the experimental target. Beamline trigger combined as follows,

$$\text{Beam} = \text{T0} \otimes \text{BHD}$$
$$\text{Kaon} = \text{T0} \otimes \text{BHD} \otimes \text{AC} \otimes \text{DEF}$$
$$\text{Pion} = \text{T0} \otimes \text{BHD} \otimes \overline{\text{AC}} \otimes \text{DEF}$$

For the $d(K^-, N)$ analysis, we made forward triggers. Forward neutral trigger was required no signal in the CVC and the PC. Forward charge trigger was defined the PC and half of the CVC which is the opposite side of beam sweeping direction. These triggers were conbimed kaon trigger and CDH 1hit trigger which is necessary to determine the reaction vertex position. CDH 2hit trigger was accumulated to evaluate that status for 2nd level trigger condition.

$$d(K^-, n)\text{main} = \text{Kaon} \otimes \text{CDH1} \otimes \text{NC} \otimes \overline{\text{CVC} \cup \text{BVC}}$$
$$d(K^-, p)\text{main} = \text{Kaon} \otimes \text{CDH1} \otimes \text{PC} \cup \text{CVC}_{\text{half}}$$
$$\text{K} \otimes \text{CDH2} = \text{Kaon} \otimes \text{CDH2}(\text{for evaluation of BVC and CVC})$$

1.6.3 DAQ live rate and trigger efficiency

We measured the DAQ live rate by the ratio of 1st trigger accepted event and request, which was plotted in Fig1.13 in MR-RUN79 as an example.
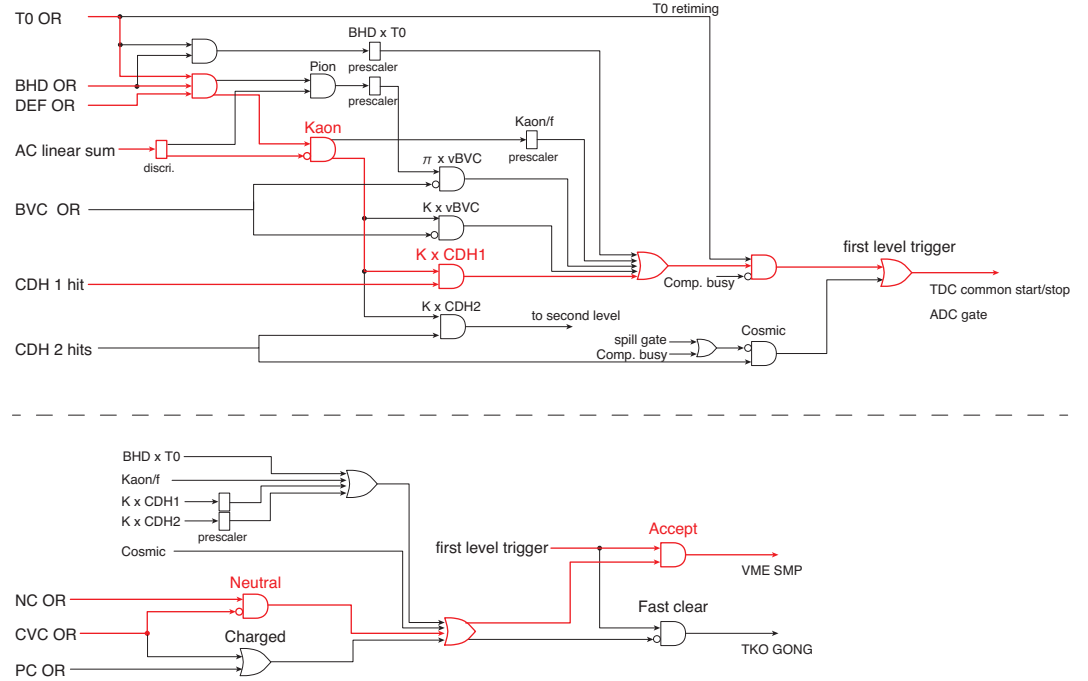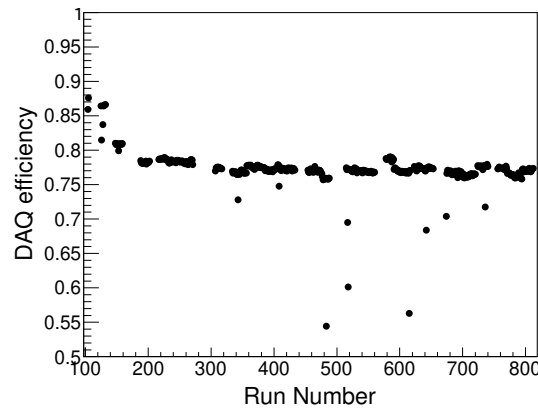
Figure 1.12:   Schematic view of trigger scheme

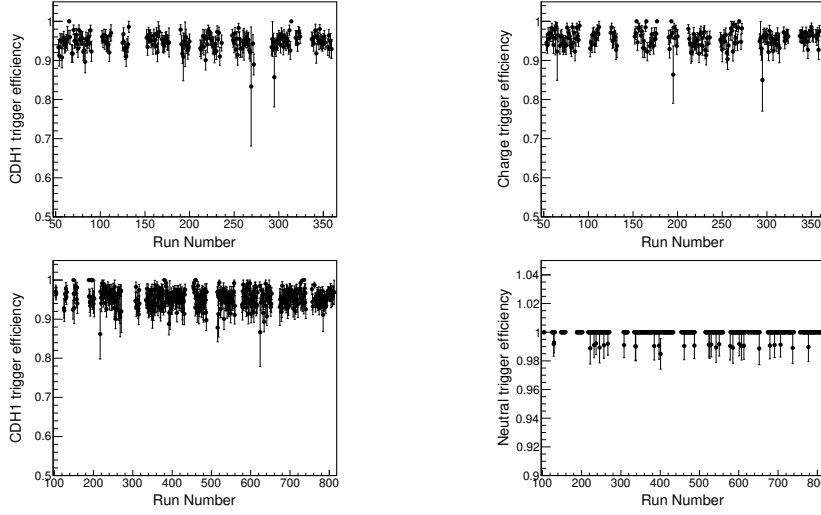Figure 1.13:   This figure shows DAQ live rate of production run in MR-RUN79.

Figure 1.14: These figures show about trigger efficiencies in each run. The $d(K^-, p)$ analysis was analyzed using MR-RUN68 data which is shown in the above. The right above shows the K $\otimes$ CDH1 trigger and the left above shows the charge trigger. The $d(K^-, n)$ analysis was analyzed using MR-RUN78 data which is shown in the down. The right down shows the K $\otimes$ CDH1 trigger and the left down shows the neutral trigger.

$d(K^-, n)$ and $d(K^-, p)$ trigger efficiencies were evaluated by the offline analysis in which trigger decomposed two-step. The first part is K$\otimes$CDH1 which was estimated using unbiased Kaon trigger. The second part is neutral=NC$\otimes\overline{\text{CVC} \otimes \text{BVC}}$ or charge=PC$\cup$CVC$_{\text{half}}$ which was estimated using the unbiased K$\otimes$CDH1 trigger which was plotted Fig1.14.

These two values were evaluated run-by-run and summed up as luminosity with irradiated kaon number which was described in section.**??**.

1.6.4 Basical calibration

Hodoscope signals were read out as ADC and TDC data and chambers were read out only TDC. TDC data was converted to time using the TDC calibrator signal which outputs two type signals, one is the start signal and the other is the stop signal. The stop signal was delayed with a periodic time constant, so these peaks were used for calibration peaks.

After that, hodoscope which has both TDC and ADC data was corrected slewing effect due to the raising of the signal as Fig1.15. The Signal with a small pulse height was slowly discriminated. This effect was calibrated using the following function.

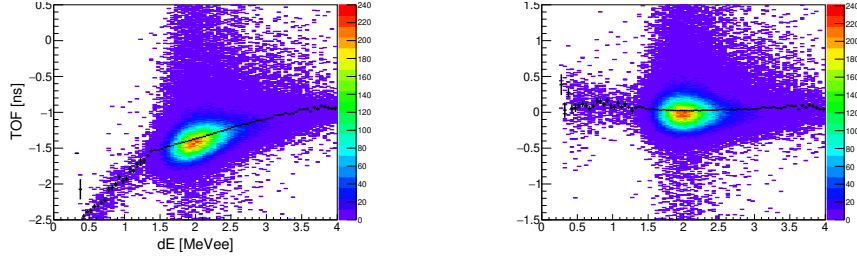$$t_{corrected} = p_0 + p_1 \frac{t}{\sqrt{dE}} + p_2 t$$

Figure 1.15:   These figures indicate about slewing effect correction. These figures show the energy deposit of the T0 as the horizontal axis and the calculated time shift of T0-NC by the   -ray as the vertical axis. The left figure shows about before correction, and the right figure shows about after correction.

This collection was performed using a well-known timing signal. For example, the Fig1.15 shows the correction of the T0 using the γ–ray peak of the T0-NC TOF which has constant velocity. This peak is also shown in Fig**??**.

Timing data of drift chambers was used to convert to the drift length. The above figure of Fig1.16 shows the drift time distribution of the drift chamber installed at the beamline. The middle figure indicates differenti- ated distribution which was used to decision start timing of each channel. The bottom figure indicates integrated distribution which corresponds to conversion map from the drift time and the drift length by assumption that beam was uniformly irradiated on.
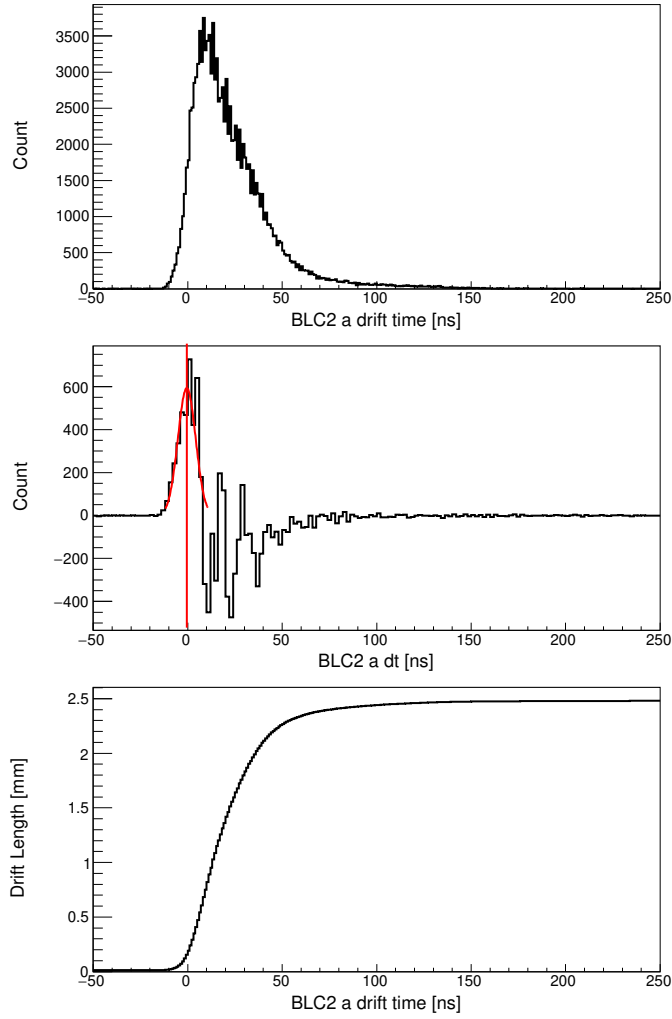
Figure 1.16:   These figures indicate the calibration of drift chambers. The above figure shows raw distribution. The middle figure shows the start timing decision which is indicated by red lines. The bottom figure shows the x-t map.

Bibliography

[1] R. H. Dalitz and S. F. Tuan, Phys. Rev. Lett. 2 (1959).
"Possible Resonant State in Pion-Hyperon Scattering"

[2] M. H. Alston, L. W. Alvarez, P. Eberhard and M. L. Good,
Phys. Rev. Lett. 6, 698 (1961).
"Study of Resonances of the $\Sigma - \pi$ System"

[3] R. H. Dalitz, T. C. Wong and G. Rajasekaran,
Phys Rev. **153**, 1617 (1967)
"Model Calculation for the $Y^*(1405)$ Resonance State"

[4] R. J. Hemingway, Nucl Phys B **253**, 742 (1985).
"Production of $\Lambda(1405)$ in $K^- p$ Reactions at $4.2\text{GeV}/c$"

[5] R. H. Dalitz and A. Deloff, J. Phys. G17, 281 (1991).
"The Shape and Parameters of the $\Lambda(1405)$ Resonance"

[6] A. D. Martin, Nucl. Phys. B **179**, 33 (1981).
"Kaon-Nucleon Parameters"

[7] J. D. Davies et el., Phys. Lett. B **83**, 55 (1979).
"Obserbation of Kaonic Hydrogen Atom X-rays"

[8] M. Izychi et el., Z. Phys. A **297**, 11 (1980).
"Results of the Search for K-series X-rays from Kaonic Hydrogen"

[9] P. M. Bird et el., Nucl. Phys. A **404**, 482 (1983).
"Kaonic Hydrogen Atom X-rays"

[10] M. Iwasaki et el., Phys. Rev. Lett. **78**, 3067 (1997).
"Observation of Kaonic Hydrogen K_α X Rays"

[11] M. Bazzi et el., Phys. Lett. B **704**, 113 (2011).
"A New Measuerment of Kaonic Hydrogen X-Rays"

[12] T. Hashimoto et el., Phys. Rev. Lett. **128**, 112503 (2022).
"Measurements of Strong-Interaction Effects in Kaonic-Helium Isotopes
at Sub-eV Precision with X-Ray Microcalorimeters"

[13] J. Zmeskal et el., J-PARC P57 Proposal
"Measurement of the Strong Interaction Induced Shift and Width of the 1s State of Kaonic Deuterium at J-PARC"

[14] N.KaiserP.B.Siegel and W.Weise, Nucl Phys A **594**, 325 (1995).
"Chiral Dynamics and the Low-Energy Kaon-Nucleon Interaction"

[15] D. Jido et el., Nucl. Phys. A **725**, 181 (2003).
"Chiral Dynamics of the Two $\Lambda(1405)$ States"

[16] Jonathan M. M. Hall et el, Phys. Rev. Lett. **114**, 132002 (2016).
"Lattice QCD Evidence that the $\Lambda(1405)$) Resonance is an Antikaon-Nucleon Molecule"

[17] H. Kamano et el., Phys. Rev. C **90**, 065202 (2014).
"Dynamical Coupled-Channels Model of K^-p Reactions:
Determination ofPpartialWwaveAamplitudes"
Phys. Rev. C**92**, 025205 (2015).
"Dynamical Coupled-Channels Model of K^-p Reactions.
Extraction of Λ^* and Σ^* Hyperon Resonances"
Phys. ReV. C**95**, 044903(E) (2015).

[18] M. Niiyama et el., Phys. Rev. C **78**, 035202 (2008).
"Photoproduction of $\Lambda(1405)$ and $\Sigma(1385)$ on the proton at $E_\gamma = 1.5$-2.4GeV/c"

[19] K. Moria for the CLAS Collaboration,
Phys. Rev. Lett. **112**, 082004 (2014).
"Spin and parity measurement of the $\Lambda(1405)$ baryon"

[20] G. Agakishiev for the HADES Collaboration,
Phys. Rev C **87**, 025201 (2013).
"Baryonic Resonances to the $\bar{K}N$ threshold: The case of $\Lambda(1405)$ in pp collisions"

[21] L.Fabbietti et el., Nucl. Phys. A **914**, 60 (2013).

[22] O. Braun et el., Nucl. Phys. B **129**, 1 (1977).
"New Information About the Kaon-Nucleon-Hyperon Coupling Constants $g(KN\Sigma(1197)), g(KN\Sigma(1385))$ and $g(KN\Lambda(1405))$"

[23] D. Jido, E. Oset and T. Sekihara, Eur. Phys. J. A **42**, 257 (2009).
"Kaonic Production of $\Lambda(1405)$ off deuteron target in chiral dynamics"

[24] K. Miyagawa and J. Haidenbauer, Phys. Rev. C **85**, 065201 (2012).
"Precise calculation of the two-step process for $K^-d \rightarrow \pi\Sigma n$ in the $\Lambda(1405)$ resonance region"

[25] S. Ohnishi et el, Phys. Rev. C **93**, 025207 (2016).
"Strcture of the $\Lambda(1405)$ and the $K^- d \to \pi \Sigma n$ reaction"

[26] H. Kamano et el., Phys. ReV. C**94**, 065205 (2016).
"Toward Establishing Low-Lying Λ and Σ Hyperon Resonances with the $\bar{K} + d \to \pi + Y + N$ Reaction"

[27] T. Hyodo and D. Jido, Prog. Part. Nucl. Phys. **67**, 55 (2012).
"The Nature of the $\Lambda(1405)$ Resonace in Chiral Dynamics"

[28] K. Agari et el, Prog. Theor. Exp. Phys., 02B009 (2012)

[29] K. Agari et el, Prog. Theor. Exp. Phys., 02B011 (2012)

[30] TRANSPORT http://linac96.web.cern.ch/Linac96/Proceedings/Thursday/THP72/Paper.p

[31] T. K. Ohska et al., Nuclear Science, IEEE Transactions on 33, 98 (1986).

[32] M. Shiozawa and et el., A new TKO system manager board for a dead-time-free data acquisition system, in 1994 IEEE Nuclear Science Symposium-NSS'94, pages 632–635, (1994)

[33] M. Iio et al., Nucl. Instrum. Methods Phys. Res., Sect. **A** 687, 1 (2012).

[34] S. Agostinelli et al., Nucl. Instrum. Methods Phys. Res., Sect. **A** 506, 250 (2003)
J. Allison et el., IEEE Transactions on Phys. Sci. 53, 207 (2006)
J.Allison et al., Nucl. Instrum. Methods Phys. Res., Sect. **A** 835, 186 (2016)

[35] K. Fuji, `https://www-jlc.kek.jp/subg/offl/lib/docs/helix_manip/node3.html` (1968).

[36] Opera Electromagnetic FEA Solution Software

[37] V. Flaminio et al., CERN-HARA-87-01, 121 (1983).

[38] M.Jones et el, Nucl. Phys. B **90**, 349 (1975)

[39] R. Barlow and C. Beeston, Comp. Phys. Comm. **77**, 219 (1993).

[40] A. Nappi, Comp. Phys. Comm. **180**, 269 (2009).

[41] M. jones, R. Levi, Setti, D. Merrill and R. D. Tripp, Phys. Rev. B**90**, 349 (1975).

[42] M. Bernheim and et. el., Nucl. Phys. A**365**, 349, (1981).

[43] R. Machleidt, Phys. Rev. C**63**, 024001 (2001).

[44] S. Agostinelli et al., Nuclear Instruments and Methods in Physics Research Section A: Accelerators, Spectrometers, Detectors and Associated Equipment **506**, 250 (2003).
J.Allison et el., Nuclear Instruments and Methods in Physics Research Section A: Accelerators, Spectrometers, Detectors and Associated Equipment **835**, 186 (2016).